

# $\gamma$ -Ray position reconstruction in large monolithic $\text{LaCl}_3(\text{Ce})$ crystals with SiPM readout

V. Babiano, L. Caballero, D. Calvo, I. Ladarescu, P. Olleros, C. Domingo-Pardo<sup>1</sup>

*Instituto de Física Corpuscular, CSIC-University of Valencia, Spain*

---

## Abstract

We report on the spatial response characterization of large  $\text{LaCl}_3(\text{Ce})$  monolithic crystals optically coupled to  $8 \times 8$  pixel silicon photomultiplier (SiPM) sensors. A systematic study has been carried out for 511 keV  $\gamma$ -rays using three different crystal thicknesses of 10 mm, 20 mm and 30 mm, all of them with planar geometry and a base size of  $50 \times 50 \text{ mm}^2$ . In this work we investigate and compare two different approaches for the determination of the main  $\gamma$ -ray hit location. On one hand, methods based on the fit of an analytic model for the scintillation light distribution provide the best results in terms of linearity and spatial resolution ( $\sim 1 \text{ mm FWHM}$ ). However, such performance is obtained only at a significant cost on reconstruction efficiency. On the other hand, position reconstruction techniques based on neural networks provide similar linearity and field-of-view, becoming the attainable spatial resolution  $\sim 3 \text{ mm FWHM}$ . For the third space coordinate  $z$  or depth-of-interaction we have implemented an inverse linear calibration approach, based on the cross-section of the measured scintillation-light distribution at a certain height. The detectors characterized in this work are intended for the development of so-called Total Energy Detectors with Compton imaging capability (i-TED), aimed at enhanced sensitivity and selectivity measurements of neutron capture cross sections via the time-of-flight (TOF) technique.

*Keywords:* gamma-ray; position-sensitive detectors; monolithic crystals; spatial resolution; neural networks;

---

## 1. Introduction

In the framework of the HYMNS (High-sensitivity Measurements of key stellar Nucleo-Synthesis reactions) project [1] we are developing radiation detectors with gamma-ray imaging capability aimed for demonstrating a novel technique [2, 3] for time-of-flight (TOF) neutron-capture cross-section measurements. The proposed detection system is based on the combination of several position-sensitive radiation detectors (PSDs) with sufficiently fast time response and good energy resolution for enabling both neutron-TOF and  $\gamma$ -ray Compton imaging techniques simultaneously. Thus, a set-up of two or more PSDs is operated in time-coincidence mode and arranged into a high-efficiency Compton imaging set-up, so called i-TED (Total Energy Detector with  $\gamma$ -ray imaging capa-

bility). Both the  $\gamma$ -ray imaging capability and the energy resolution are expected to provide a significant improvement in sensitivity and selectivity for true capture events with respect to commonly used systems [4], as described in Ref. [2]. For the implementation of the Compton technique in i-TED one needs high precision on both energy and position of the measured  $\gamma$ -ray interactions. In order to achieve this, the present i-TED design [2] comprises PSDs based on large monolithic  $\text{LaCl}_3(\text{Ce})$ -crystals optically coupled to pixelated silicon photomultipliers (SiPMs). In a previous recent publication [5] we investigated in detail the spectroscopic performance of the PSDs. In this work we evaluate the performance of several algorithms to reconstruct the 3D-coordinates for the main  $\gamma$ -ray hit in the scintillation crystal.

There exist many position reconstruction algorithms for

monolithic crystals available in the literature. First approaches for 2D position reconstruction, such as the centroid or Anger-logic technique [6, 7], use the mean value of the charge distribution collected on the photosensor (or an array of sensors) in order to infer the position of the main  $\gamma$ -ray hit in the transversal XY-plane of the scintillation crystal. This approach is commonly embedded by means of a resistor-network. The latter can also provide a certain sensitivity for the third spatial coordinate ( $z$ ) or depth-of-interaction (DoI) [8]. In continuous scintillation crystals the centroid-approach works well only in the central region of the PSD, where the collected charge distribution is still rather symmetric and reflection effects in the crystal-walls have a small influence. However, strong compression or “pin-cushion” effects take place in the peripheral region of the PSD, thus severely reducing the FoV and linearity of the system. This can be cured, to some extent, by so-called weighted centroiding methods [9]. Also, enhanced linearity and spatial resolution have been demonstrated by the squared-charge centroiding technique reported in Ref. [10].

Over the last decade there have been many advances in terms of instrumentation for PSDs. On the one hand, the latest generation of fast and high-photon yield halide crystals [11, 12, 13, 14] coupled to pixelated p-on-n semiconductor photosensors have opened up a new scope of possibilities and applications [15, 16]. On the other hand, the revolutionary monolithic concept [17] has eventually led to compact multi-channel photosensor-readout application-specific integrated circuits (ASICs), which enabled the possibility to build high granularity, scalable and large arrays of PSDs. For a few examples see e.g. Refs. [18, 19, 20].

Thanks to these developments, most modern position-reconstruction algorithms implement an individual multi-channel scheme for the readout of the PSDs, thereby following the concept introduced by Bird et al. [21] in 1994. Presently, the former phenomenological Gaussian-based peak-fitting algorithms for position reconstruction [22] have been superseded by more realistic theoretical models for the scintillation-light distribution [8, 23, 24]. The latter provide indeed a better representation of the measured detector response, as reported e.g. in Refs. [25, 24, 26]. The main advantage of the analytic approach resides on the fact that, a priori, only a few parameters need to be empirically characterized. Thus, using  $20 \times 20 \times 10 \text{ mm}^3$

LSO crystals coupled to  $8 \times 8$ -pixels SiPMs spatial resolutions of 1.4 mm FWHM at 511 keV have been reported [24]. However, due to the theoretical nature of this methodology, experimental set-up particularities such as imperfections in the finishing of the PSDs, inhomogeneities in the crystal or in the optical coupling to the photosensor, fluctuations in the gain response for different channels, etc are not directly taken into account. Another limitation of such algorithms may arise for applications which require a real-time position reconstruction due to the relatively lengthy minimization process. For neutron capture experiments, however, where typically offline analysis of the capture data is carried out, this does not represent any drawback.

Experimental details in the PSD response may be more reliably accounted for by means of an exhaustive characterization of the spatial detector response for all possible  $\gamma$ -ray interaction positions. This kind of pattern-shape analysis has been implemented with a great level of detail by means of algorithms such as the  $k$ -NN technique [27, 28, 29]. The latter is based on a large database of measured 2D-reference patterns, which are then used in the position-reconstruction algorithm to determine the 3D-location of the main  $\gamma$ -ray hit. For  $50 \times 50 \times 30 \text{ mm}^3$   $\text{LaBr}_3$ -crystals spatial resolutions of 4.5 mm FWHM at 662 keV have been reported [30] for the so-called “Categorical Average Pattern” extension of the aforementioned  $k$ -NN algorithm.

Finally, progress on computing power has also enabled the possibility to apply machine-learning artificial neural-network (NN) algorithms to the problem of the position reconstruction [31, 32, 33, 34, 35]. In this case also a large database of detector responses is required, either simulated [33] or experimentally determined [35], in order to train and test the network. Thus, at 356 keV, spatial resolutions of 2.9 mm FWHM and 8 mm FWHM for  $25 \times 25 \times 10 \text{ mm}^3$   $\text{CeBr}_3$  and  $28 \times 28 \times 20 \text{ mm}^3$   $\text{LaBr}_3$  crystals coupled to  $4 \times 4$  pixels SiPM, respectively, are reported in Ref. [35]. Using larger crystals of  $50 \times 50 \times 10 \text{ mm}^3$  volume coupled to  $8 \times 8$  multi-anode photomultiplier-tubes (PMTs), resolutions of  $\gtrsim 2 \text{ mm RMS}$  ( $\gtrsim 4.7 \text{ mm FWHM}$ ) are reported in Ref. [33].

In this work we explore the applicability and performance of some of these methods to three large monolithic  $\text{LaCl}_3(\text{Ce})$ -crystals, with a base surface of  $50 \times 50 \text{ mm}^2$  and thicknesses of 10 mm, 20 mm and 30 mm. To our

knowledge, these are the largest lanthanum-halide monolithic PSDs with SiPM readout aimed at  $\gamma$ -ray imaging reported in the literature thus far. The pixelated SiPMs, readout- and processing-electronics together with the characterization apparatus and methodology are described in Sec. 2. The implemented position reconstruction algorithms are reported in Sec. 3. The latter section is divided in three parts. The first part (3.1) describes the performance of two common methods, namely the Anger logic [6], and the squared-charge centroiding approach [10]. These basic methods have been implemented in this work with the purpose of defining the main performance figures of merit, such as resolution, linearity, field of view (FoV) and signal-to-noise (S/N) ratio. Due to their simplicity, they are still among the fastest algorithms for online monitoring during a measurement and thus, we use them in this work to benchmark the speed-capability of more sophisticated approaches. The second sub-section (3.2) describes the performance of state-of-the-art analytic models for the propagation of the scintillation photon field within the crystal, applied to the position reconstruction along the transversal  $xy$ -plane. Hereby the simple model by Lerche et al. [8] is compared against the more elaborated model by Li et al. [24]. In Section 3.3 we describe the implementation and performance of NN-algorithms, also constrained to the transversal crystal plane. As reported in Sec. 4 we have found better results by decoupling the transversal position reconstruction (either with analytic or NN-methods), from the reconstruction in  $z$  or DOI. The latter section thus describes the methodology implemented here for the reconstruction of the third space coordinate. A general comparison summarizing the advantages and drawbacks of each method is reported in Sec. 5.

## 2. Apparatus and experimental set-up

### 2.1. $\gamma$ -Ray position sensitive detectors (PSDs)

We characterize three planar monolithic scintillation crystals of  $\text{LaCl}_3(\text{Ce})$ , all of them with a base surface of  $50 \times 50 \text{ mm}^2$  and thicknesses of 10 mm, 20 mm and 30 mm. All crystals are encapsulated in a 0.5 mm thick aluminum housing, which is isolated from the crystal itself with a 1 mm thick seam gum. The base of the crystal is optically coupled to a fused-silica glass window of

2 mm thickness. Apart from the polished base surface of the crystal, the other five surfaces are ground finished and covered with diffuse polytetrafluoroethylene reflector (PTFE) to optimize photon-collection.

Each scintillation crystal is optically coupled with silicon grease (BC-630) to a silicon photomultiplier array (SiPM) from sensL (ArrayJ-60035-65P-PCB). This monolithic sensor has a size of  $50.44 \times 50.44 \text{ mm}^2$  and features  $8 \times 8$  pixels, each one with a size of  $6 \times 6 \text{ mm}^2$  on a pitch of 6.33 mm. Each pixel features 22292 avalanche photodiodes (APDs) or micro-cells ( $35 \mu\text{m}$  size) and the fill-factor is of 75%. These APDs are built using a p-on-n semiconductor structure, thus featuring the maximum of the photodetection efficiency at relatively low photon wavelengths ( $\sim 420 \text{ nm}$ ), which still matches reasonably well with the main emission wavelength of 350 nm for  $\text{LaCl}_3(\text{Ce})$ . For more information the reader is referred to Ref.[36]. For further details about the energy resolution and spectroscopic performance of these PSDs the reader is referred to Ref. [5].

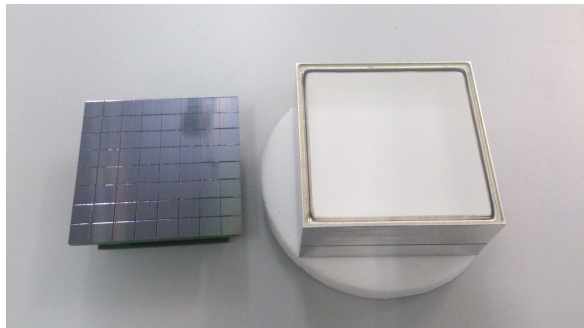


Figure 1: Photograph of the 20 mm thick  $\text{LaCl}_3(\text{Ce})$  crystal together with the  $8 \times 8$  pixel sensL SiPM.

### 2.2. Frontend SiPM readout and bias electronics

The SiPMs are biased and readout by means of the PETsys TOF Front-End Board D version 2 (FEB/D-1024) [37]. The chosen reverse bias voltage is of +5 V beyond the nominal breakdown value of 24.5 V, corresponding to a nominal quantum efficiency of nearly 50%/microcell. For the present measurements we use two of the eight acquisition ports available at the motherboard FEB/D\_v2, each port capable of acquiring up to 128 individual SiPM signals. The analogue signals are read-

out via 64-channel frontend ASICs (TOFPET2), which are plugged by means of a customized PCB-board to the Samtec 80-way connectors (QTE-040-03-F-D-A) at the rear-side PCB of each SiPM. The ASIC performs the readout and digitization of the SiPM signals and uses a low threshold for timing and a high threshold for accepting the event. The input dynamic range is of 1500 pC. Every time one of the 64 channels exceeds the high threshold a record is created giving the channel number, the time and the charge of the event. Digitized events contain the signal integrated charge and time stamp, and are sent via 50 cm long Samtec EQCD High-Speed flat cables to the FEB/D\_v2 motherboard, where a Kintex7 FPGA performs further event pre-processing. The communications-mezzanine sends the processed data (time-stamp, qdc and pixel identification number) via a fast Gigabit ethernet link to the acquisition computer running the system-control, bias and online monitoring software. Data are stored in binary files with a convenient format, for posterior event-building and time-coincident event selection.

Both the SiPM and the TOFPET2 chips are sensitive to temperature variations and thus, a cooling system was implemented in order to keep stable thermal conditions and to constantly monitor the temperature. To this aim cooled and compressed air (1.3 bar) is constantly flushed onto the ASIC surface by means of a customized encapsulation and a tube with a diameter of 4.5 mm pointing to the ASIC. The air is cooled using a system build with four Peltier cells connected to a thermal isolated aluminum case. The hot Peltier surface is thermally coupled to a 1 cm thick heatsink block of aluminum, which is refrigerated by means of a water assisted cooling system (Kraken x52 by NZXT). Temperature is monitored with a  $\pm 0.1$  K accuracy at different points using 100K thermistors connected to the main acquisition computer through an Arduino controller board. Temperature is monitored inside the cooler-case, at the hot area of the aluminum block and inside each detector housing. In such locations, the typical stable temperature during acquisition is 12°C, 50°C and 21.5°C, respectively.

### 2.3. Scanning table and data-sets

For the systematic scan of the full detector surface we use an XY table from ARRICK-ROBOTICS [38] equipped with a low-stretch timing belt and stepper motors. The original system for controlling the stepper motors used an

outdated parallel printer-port. For convenience we replaced them with a self-made control unit based on the Atmega328P microcontroller embedded in an Arduino Nano board, which is controlled from the computer via USB connection. The interface includes drivers (ULN2004) for the stepper motors and a 12 V DC-supply voltage. The drivers are mounted with a small heatsink and the temperature is also monitored. Each of the two stepper motors for X and Y positioning is connected to a 2.5:1 pulley reducer, which enables a positioning resolution of about 80  $\mu\text{m}/\text{step}$  and a repeatability of 0.2 mm. This accuracy was checked by means of a digital microscope and a calibration slide. The XY-positioning is synchronized with our acquisition system (see below) in order to trigger and stop data-taking and to store data-files with proper names indicative for the scanning position of each acquisition. To this aim a software code was written, which reads a user-provided configuration file with a series of position coordinates  $x$  and  $y$ , and the acquisition time preset for each location.

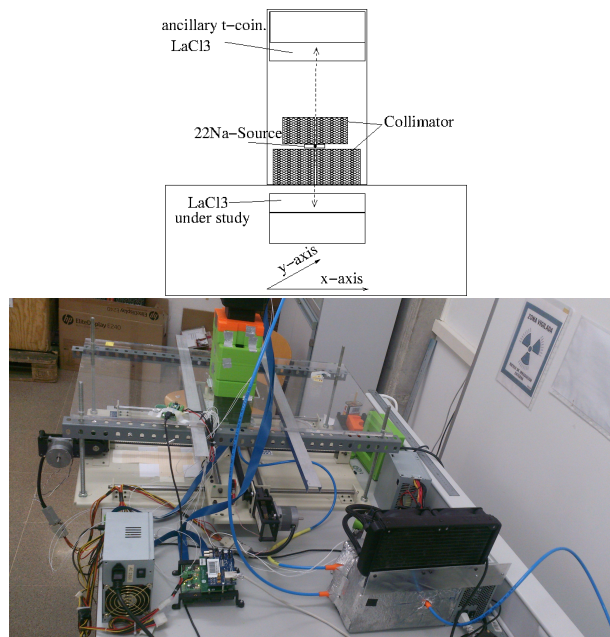


Figure 2: The characterization workbench with XY scanning-table. The two  $\text{LaCl}_3(\text{Ce})$  detectors are mounted in vertical position, as illustrated in the schematic drawing. The detector at the top remains fixed and coupled to the collimated  $^{22}\text{Na}$  positron source. The bottom detector sits on the movable XY-bench for characterization.

In order to suppress the self-activity of the  $\text{LaCl}_3(\text{Ce})$  scintillation crystals all measurements were made in time-coincidence between two detectors using the 511 keV annihilation gamma-quanta emitted isotropically in back-to-back direction from a point-like  $^{22}\text{Na}$ -source with an activity of 0.2 kBq. The coincidence time-window was set to 20 ns. The PSD under characterization was attached to a small movable platform, whereas the collimator, the  $^{22}\text{Na}$ -source and the ancillary detector were fixed on top of a 10 mm thick platform from Plexiglas (see Fig. 2). The collimator is a parallelepiped made from tungsten, with a central hole-diameter of 1 mm and a thickness of 30 mm.

A total of three data-sets were acquired, one for each crystal. Each data-set is composed of a matrix of  $35 \times 35$  collimated positions on a pitch of 1.5(1) mm. The scanned positions are schematically represented in Fig. 3. Data were acquired for each scan position during a time interval of 600 s. The scan of each detector thus lasted about 8 days.

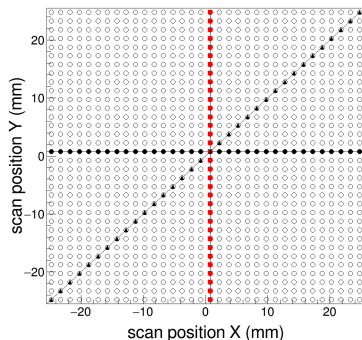


Figure 3: Schematic drawing of the  $35 \times 35$  scan positions on a pitch of 1.5 mm (open circles). Solid symbols are displayed for the proper interpretation of the linearity curves described in the sections below.

Hereafter, the 35 collimated positions along central  $x$ -axis of the PSD (solid black circles in Fig.3) and the 35 positions along the orthogonal  $y$ -axis (solid red circles) are referred to as horizontal and vertical scanning lines or central cross. The 35 collimated positions (solid triangles) depicting a  $45^\circ$  line with respect to the previous two directions are referred to as diagonal scanning line.

#### 2.4. Deconvolution of the collimated $\gamma$ -ray beam divergence

In order to determine the intrinsic detector spatial resolution from a measurement made with a collimated  $\gamma$ -ray source it becomes necessary to deconvolute the spatial spread. Apart from the intrinsic detector and reconstruction algorithm resolutions, the overall broadening is mainly determined by the collimator aperture, the thickness and the distance to the detector under study. To this aim we have carried out Monte Carlo (MC) simulations using the GEANT4 code [39]. The experimental set-up was included in the simulation and special care was taken to model in a realistic way all sensible distances and materials. For each crystal thickness a total of  $1 \times 10^9$  events from an isotropic source of 511 keV  $\gamma$ -rays were simulated. One example for the position spread in the 20 mm thick crystal is given below in Fig. 4.

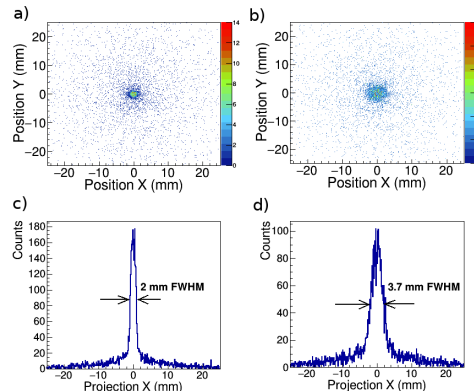


Figure 4: MC simulation for 511 keV  $\gamma$ -rays passing through the 1 mm diameter collimator and impinging at the center of the 20 mm thick  $\text{LaCl}_3(\text{Ce})$  detector (see text for details). Figures a) and b) show the simulated 2D-distribution for an ideal detector and for a detector with an intrinsic resolution of 3 mm FWHM, respectively. The bottom panels c) and d) show the corresponding projections over the  $x$ -axis, thus yielding an intrinsic set-up related broadening of 2 mm FWHM and an overall broadening (detector/algorithm plus set-up) of 3.7 mm FWHM.

To determine the relation between the “true” or intrinsic detector spatial resolution and the total or “measurable” width, for each simulation we convolute the simulated positions of the  $\gamma$ -ray hits with a Gaussian function. This convolution is carried out for a series of Gaussian widths spanning from 0 mm up to 22 mm FWHM. The result for the 20 mm thick crystal is displayed in Fig. 5, which

shows the dependency between the convolution width or instrumental resolution versus the overall (divergence affected) distribution width. For convenience the simulated data-points are adjusted to an arbitrary polynomial function, which is then used along this work in order to derive the intrinsic detector resolution from the total measured width.

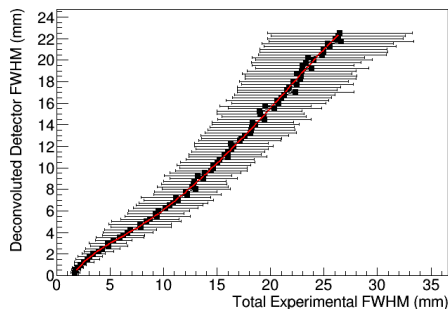


Figure 5: Deconvolution function obtained from the MC-simulated and convoluted responses for the 20 mm thick  $\text{LaCl}_3(\text{Ce})$  crystal.

For the sake of clarity, results are exemplified here only for the 20 mm thick  $\text{LaCl}_3(\text{Ce})$  crystal. Similar calculations were also carried out for the other two crystal thicknesses of 10 mm and 30 mm and applied consequently along the work for deconvoluting the intrinsic detector resolution.

### 3. $\gamma$ -Ray position reconstruction algorithms

This section is structured as follows. Sec. 3.1 describes briefly two of the most common reconstruction techniques, namely the Anger-logic method [6, 7] and a variation of it, the so-called squared-charge centroiding approach [10]. The performance of these algorithms is in actuality superseded by other techniques, such as those reported in the subsequent sections. Nevertheless we have implemented these two basic position-reconstruction methods in order to define the main performance figures of merit used along this work, and to illustrate the improvement attained with more modern apparatus and approaches. On the other hand, owing to the simplicity of these methods, they are the fastest from the computational point of view and thus, serve as reference for benchmarking the computational load of the other methods. State-

of-the-art algorithms like those based on analytic models and artificial NNs are reported in Sec. 3.2 and Sec. 3.3, respectively. For all algorithms only events with a full-energy deposition are taken into account.

#### 3.1. Anger-logic and squared-charge techniques

In order to emulate the centroiding approach instead of hardware implementing a resistor network we follow a software approach, which is based on the computation of the mean-value of the charge-distributions measured with our pixelated SiPMs. Similarly, the mean value of the squared-charge distribution is also used to implement the squared-centroiding method [10]. As illustrative reference, position-reconstruction examples for the central scan position of true coordinates ( $x_{true} = 0 \text{ mm}, y_{true} = 0 \text{ mm}$ ) and a peripheral scan position ( $x_{true} = 21 \text{ mm}, y_{true} = 21 \text{ mm}$ ) acquired for the 20 mm thick  $\text{LaCl}_3(\text{Ce})$  crystal are shown below in Fig. 6 and Fig. 7 for both algorithms. By comparing these distributions the enhancement in FoV obtained with the second approach becomes directly apparent.

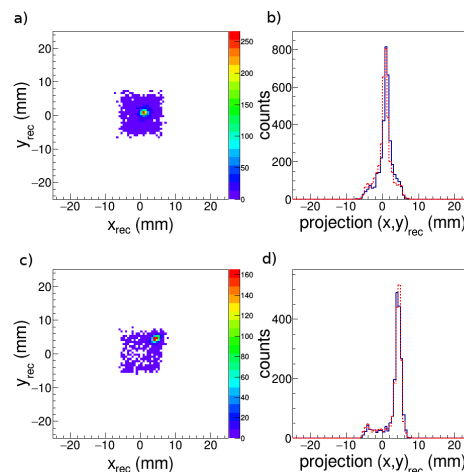


Figure 6: Event-by-event reconstructed 2D-locations using the Anger-logic technique for the central scan position (a). The panel (b) shows the projected position distribution over the  $x$ -axis (solid line) and over the  $y$ -axis (dashed line). Panels (c) and (d) show equivalent distributions for a scan position shifted 21 mm in  $x$  and  $y$  with respect to the center, i.e. towards the top-right crystal corner.

The linearity curve, defined here as the relation between the mean value of the reconstructed positions and

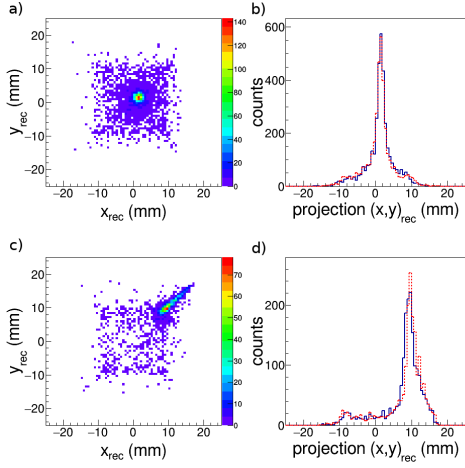


Figure 7: Same as Fig. 6 using the squared-charge centroiding method [10].

the true position for each scanned point is shown in Fig. 8 for the central cross of 35-horizontal and 35-vertical scanning positions. These 69 positions (note that the central position is common to both data-sets) are those represented in Fig.3 by solid black circles and solid red squares, respectively. The thin-dashed line shows the behavior expected for an ideal detector. Deviations between reconstructed and true positions are displayed in the bottom panels. Thus, the slope of the linearity curve in the central linear region provides a measure of the quality of the algorithm in terms of image compression. Already in this central part the slope of the linearity curve is of only 30(1)% for the Anger-logic approach. The spatial resolution, defined as the FWHM-value of the x (y) projected-distribution for the reconstructed positions along the x (y) axis are shown in Fig.9; Along the central cross of scan positions the average resolution is of 10.8(6) mm FWHM. These values include also a correction for the aforementioned linearity distortion.

A significant improvement in linearity and resolution is obtained simply by working with the squared-charge values of each pixel, as reported in Ref. [10]. This is demonstrated in Fig. 8, which shows an improved average linearity of 51(1)% along the x- and y-axis. The average spatial resolution is of 7.3(6) mm FWHM. Nevertheless, the spatial response is still remarkably affected by border effects. Fi-

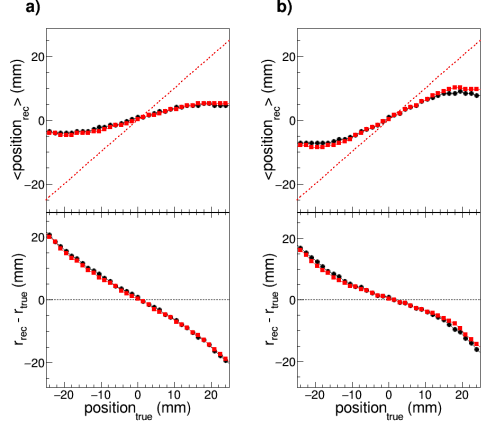


Figure 8: Linearity obtained with the Anger-logic technique (a) and the squared-charge method (b) for scan positions along the central x-axis (black circles) and y-axis (red squares) of the crystal.

nally, it is worth noting that the linearity curves displayed in Fig. 8 are quite similar to the comparison reported in Fig. 3 of Ref.[10], thus in agreement with the software-approach implemented here.

The field-of-view (FoV), defined here as the sensitive PSD surface where the linearity curve along the x- and y-axes shows a strictly increasing behaviour, can be determined from the diagrams above to be of about  $30 \times 30 \text{ mm}^2$  and  $40 \times 40 \text{ mm}^2$  for the Anger and for the squared-charge centroiding methods, respectively. Despite of their limited performance, a clear advantage of these methods is their reconstruction speed. Using a computer with a core i7 from Intel, processing rates of  $r_{Anger} = 6840 \text{ Events/s}$  and  $r_{Q^2} = 6647 \text{ Events/s}$  were obtained for the Anger- and squared-charge centroiding techniques, respectively. The value of  $r_{Anger}$  will be used in the rest of this work in order to benchmark the processing-speed performance of the other methods.

### 3.2. Analytic model fit

There exist several analytical models to describe the 3D-spatial propagation of the scintillation photons produced by a single  $\gamma$ -ray hit or, equivalently, by a point-like photon source within the crystal volume [8, 23, 24]. Here we report on the implementation of algorithms based on both the model by Lerche et al. [8] and the somewhat more elaborated formula by Li et al. [24]. The Lerche

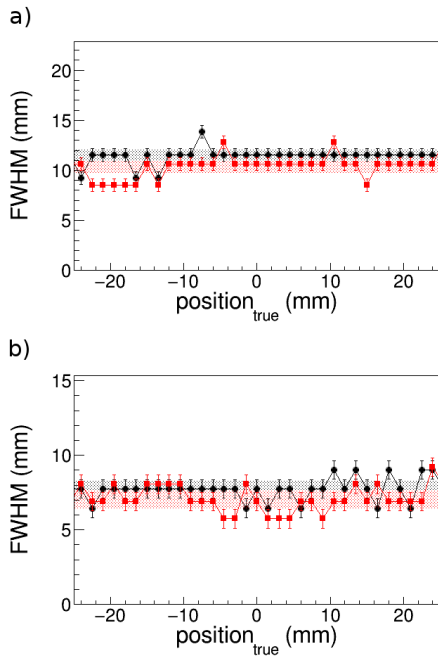


Figure 9: Spatial resolution  $\text{FWHM}$  obtained with the Anger-logic technique (a) and for the squared-charge centroiding method (b) for scan positions along the central  $x$ -axis (bold-circles) and  $y$ -axis (red-squares) of the crystal. Shaded bands represent average resolution values in the detector FoV.

model makes use of the inverse square law combined with an exponential factor, which accounts for photon absorption and scattering effects within the crystal. An additional constant term is used to take into account the scintillation-light or electronic-noise background. Two parameters  $L_0$  and  $\alpha$  account for the intensity of the photon source and for the average absorption, respectively. Using a dedicated flood-illumination measurement for each crystal we determine these two parameters empirically and fix them to their mean value.

The model by Li includes additional effects of photon-reflection on the walls of the crystal, a feature which seems convenient in our case due to the PTFE reflector wrapping our crystals (see Sec. 2). Additionally a cut-off factor  $\beta$  is used to describe the crossover from the refractive to the reflective regime. The exact value for this parameter has a small impact on the results and, as recommended [24], we set it to a value of  $\beta = 100$ .

To implement these algorithms, the PSD charge-response measured with the SiPM is stored on an event-by-event basis in a 2D-histogram, which is then fitted to the corresponding formula (Lerche or Li) using the log-likelihood method. For this we make use of the `TMinuit` minimization class of the CERN ROOT package [40]. The method allows one to use the value of the fit  $\chi^2$  in order to reject events where the model is not reproducing well the measured charge distribution. This situation may happen rather frequently depending on crystal material and energy of the  $\gamma$ -quanta, when the registered event is made from a sequence of multiple Compton  $\gamma$ -ray hits inside the crystal, eventually leading to full-absorption. Examples of  $\chi^2$  distributions are shown and discussed below.

#### *LaCl<sub>3</sub>(Ce) 50×50×10 mm<sup>3</sup>*

Fig. 10 shows an example of a random event measured at the center of the 10 mm thick crystal and fitted using the Lerche model. The suitability of the analytical model for the measured data can be estimated on the basis of the  $\chi^2$ -distribution obtained from the fit. One example of the  $\chi^2$  distribution obtained with the Lerche model for all events in the central collimated position of the 10 mm thick crystal is given in Fig. 10-(b). Similar distributions are obtained for other scan positions, and for the Li model as well. We have carried out a systematic study of the performance attainable for the position reconstruction as

a function of the cut or selection in the  $\chi^2$ -distributions. A reasonable solution seems to use the 50% of events with best (lowest)  $\chi^2$  value, and this is what we use along this work unless otherwise stated. Obviously the best balance between reconstruction efficiency and performance can be determined for each specific application.

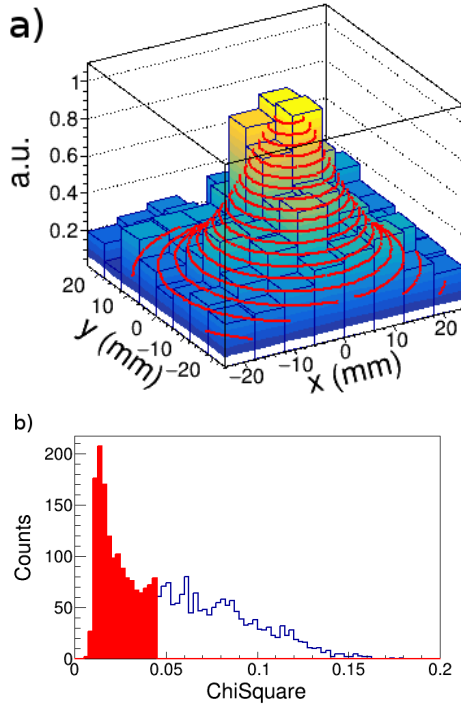


Figure 10: Example of an arbitrary measured distribution fitted to the Lerche-model (a). Panel (b) shows the  $\chi^2$  distribution for all events accumulated and fitted in a central scan position. The filled region indicates the events chosen as good candidates for the position reconstruction. See text for details.

The reference examples of spatial distributions are shown in Fig. 11 and Fig. 12 for the Lerche and Li models, respectively. The represented positions,  $(x_{true} = 0 \text{ mm}, y_{true} = 0 \text{ mm})$  and  $(x_{true} = 21 \text{ mm}, y_{true} = 21 \text{ mm})$ , are the same as those shown in Fig. 6 and Fig. 7 for the centroiding approaches.

In order to reliably quantify the size and the geometry of the FoV one needs to consider that light-reflection effects become more acute at the corners of the crystal than in the central wall region between corners. A position-fit reconstruction algorithm can be very sensitive to such

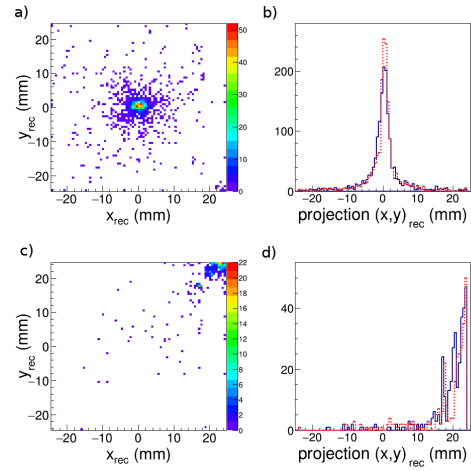


Figure 11: Examples for central (a-b) and peripheral (c-d) scan positions as reconstructed with the Lerche-fit method.

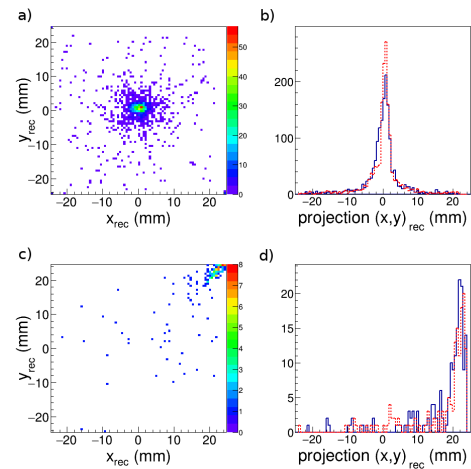


Figure 12: Same examples as those shown in Fig. 11 using the Li-fit method.

effects and, therefore, it becomes convenient to evaluate the linearity of the system not only along the central  $x$ - and  $y$ - axis, but also along the diagonal of the PSD (see Fig. 3). Thus, the linearity curves for both the diagonal scan and for the central cross along the  $x$ - and  $y$ -axis are displayed below in Fig. 13 and Fig. 14, respectively.

Using the Lerche (Li) model we find a linearity range of 40.5 mm (43.5 mm) and 46.5 mm (46.5 mm) along the crystal diagonal and central-cross of scanned positions, respectively (see Fig. 13 and Fig. 14). The slightly better performance by the Li-model can be most probably ascribed to the contribution of light-reflection effects. In general, we find that the FoV is limited by the linearity performance along the diagonal. Therefore we use the diagonal scan to define the size of a square-linear FoV. Thus, for the 10 m thick crystal we obtain a FoV of 16.4 cm<sup>2</sup> and 18.9 cm<sup>2</sup> for Lerche- and Li-models, respectively. Within the quoted FoV the linearity is practically 100%, with root-mean-square (RMS) deviations of  $\lesssim 0.9$  mm for both models (see Table 1).

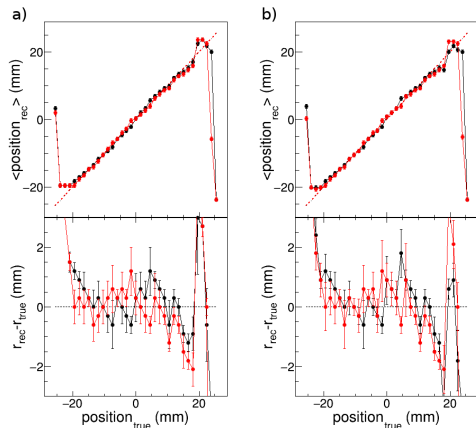


Figure 13: Linearity along the diagonal of the 10 mm thick crystal for the Lerche-fit (a) and Li-fit (b) methods.

In terms of spatial resolution the performance of both Lerche- and Li-models is quite similar, with average values of  $\sim 1.2$  mm FWHM, as summarized below in Table 1.

Finally, another important aspect to quantify the overall performance of the position-reconstruction algorithm is the S/N-ratio. For the present study we define the S/N as the density of events within full-width-at-tenth of

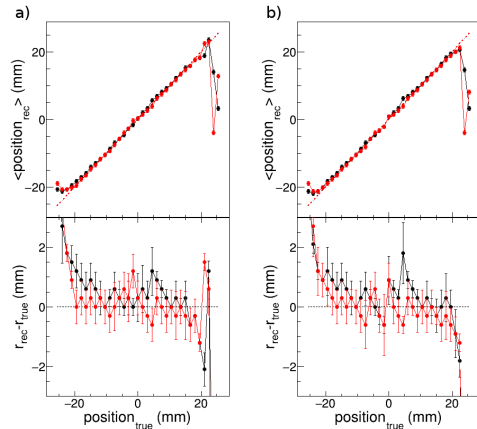


Figure 14: Linearity along the diagonal set of scan positions in the 10 mm thick crystal using the Lerche-fit (a) and Li-fit (b) methods.

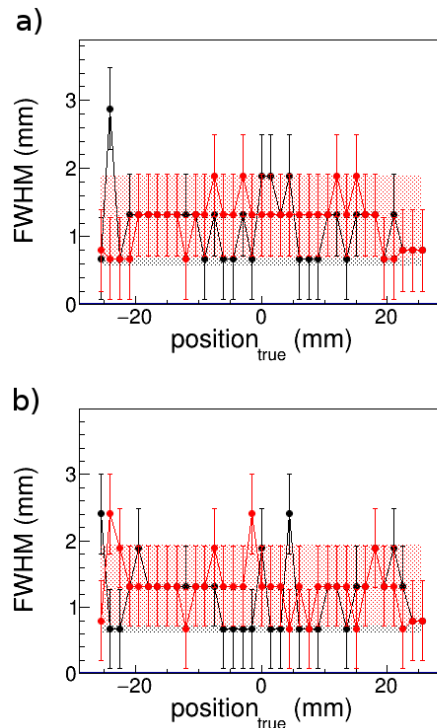


Figure 15: Spatial resolutions FWHM obtained with the Lerche-model fit (a) and Li-model fit (b) for the 10 mm thick crystal.

the maximum (FWTM) for the 2D-distribution, normalized by density of “stray” events outside that region. For the 10 mm thick crystal we obtain average S/N ratios of 14(3) and 12(5) for the Lerche and Li models, respectively (see Table 1).

*LaCl<sub>3</sub>(Ce) 50×50×20 mm<sup>3</sup>*

The results obtained with both analytical methods for the 20 mm thick crystal are quite similar to those found before for the thin crystal. The linearity (see Fig. 16) seems slightly better than for the 10 mm thick crystal, with FoV values of 18.9 cm<sup>2</sup> and 21.6 cm<sup>2</sup> for the Lerche- and Li-fit methods, respectively. The resolution (Fig. 17) deteriorates only slightly, with average values of ~1.3 mm FWHM.

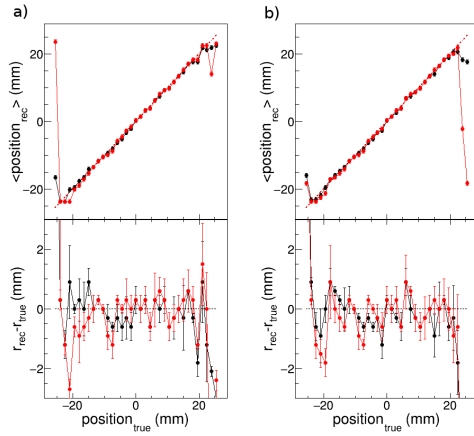


Figure 16: Linearity for the diagonal positions along the 20 mm thick crystal with the Lerche-fit (a) and Li-fit (b) methods.

*LaCl<sub>3</sub>(Ce) 50×50×30 mm<sup>3</sup>*

In this case the choice of a  $\chi^2$  threshold for 50% reconstruction efficiency leads to rather poor linearity results. Therefore, for the 30 mm thick crystal we apply a more restrictive  $\chi^2$ -cut to select only 20% of the events with lowest  $\chi^2$  (see Fig. 18). In this way, linearity and resolution remain quite similar to that of the thinner crystals (see Fig. 19 and Fig. 20). The FoV becomes of 21.6 cm<sup>2</sup> for both Lerche- and Li-fit methods.

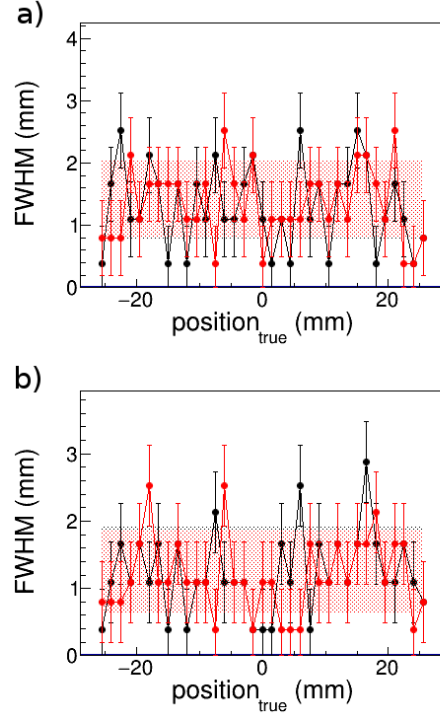


Figure 17: Spatial resolution FWHM (mm) obtained for the 20 mm thick crystal using the Lerche- (a) and Li-model (b) fit methods.

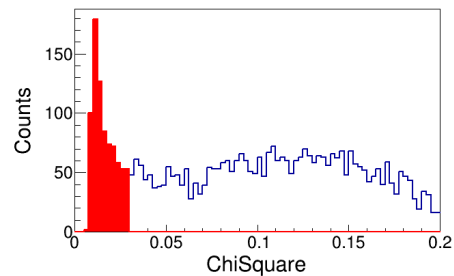


Figure 18:  $\chi^2$ -distribution for the 30 mm thick crystal in the central scan position using the Li-method.

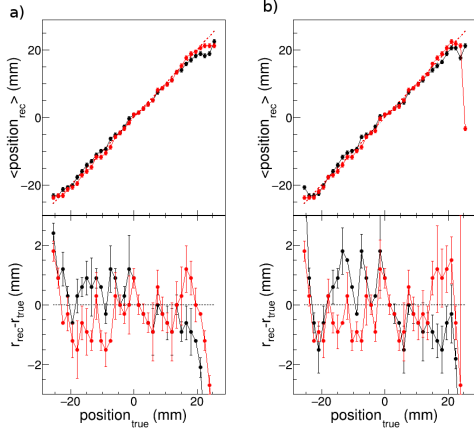


Figure 19: Linearity for the Lerche-fit (a) and Li-fit (b) methods applied to the 30 mm thick crystal.

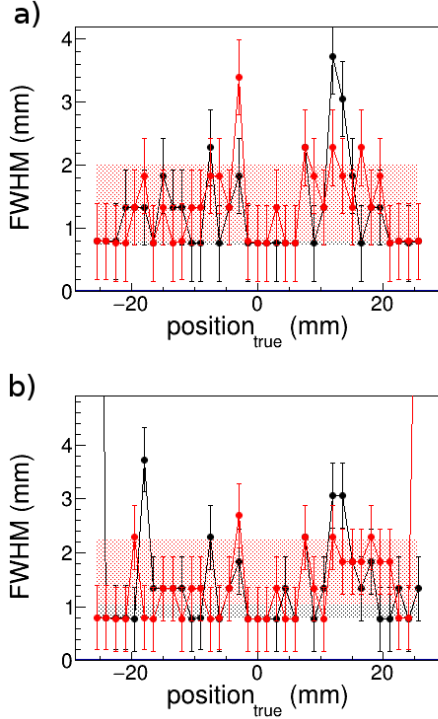


Figure 20: Spatial resolution obtained with the 30 mm thick crystal using the Lerche-model (a) and the Li-model (b).

### Summary of performances obtained with the analytic-fit methods

The most remarkable feature of these methods is the spatial accuracy of  $\gtrsim 1$  mm FWHM. Interestingly, this spatial resolution can be achieved for all crystal thicknesses and with only a minor previous characterization. However, such an accuracy seems feasible only at a rather expensive cost on reconstruction efficiency. Resolution, linearity and FoV show a remarkable improvement with respect to the Anger- and squared-charge centroiding approaches. In particular, the FoV remains practically constant for the Li-method regardless of the crystal thickness, whereas a systematic positive trend is observed for the Lerche-method (see Table 1). This effect indicates that the aspect-ratio of the crystal has a significant effect in the reflection effects, which is properly accounted for within the Li-model. The S/N-ratio shows a systematic deterioration as a function of the crystal thickness, which seems more acute for the Li-method. This feature points to a better suitability of analytical models for the position reconstruction in thin crystals ( $\sim 10$  mm). Indeed, the information available about the applicability of such techniques to thick scintillation crystals is rather scarce or inexistent.

It is worth noting that the rate-processing speed is more than a factor of two faster for the Lerche-model approach ( $r_{\text{Lerche-fit}} = 2433$  Ev/s) than for the Li-method ( $r_{\text{Li-fit}} = 967$  Ev/s). This can be ascribed to the simpler mathematical expression and lower number of variables. Such processing rates represent only 35% and 14% of the benchmark value  $r_{\text{Anger}}$  (see Sec. 3.1), respectively.

### 3.3. Artificial Neural Network

To implement a NN-algorithm for the position reconstruction we make use of the Multi-Layer-Perceptron class library (TMultiLayerPerceptron) of the CERN ROOT package. From the different learning-methods available in this class, we find the quasi-Newton approach by Broyden-Fletcher-Goldfarb-Shanno (BFGS) to be the one providing best results. Similarly as reported in Ref. [35], we also find noticeably better results when two decoupled and independently trained NNs are used, one for the  $x$ -coordinate and another one for the  $y$ -coordinate, rather than a single network with two outputs ( $x, y$ ). With our 64-channel SiPMs, the NN input is always a 64 neuron passive-layer, which represents the charge-content of

Table 1: Summary of performances obtained with the two analytical models for the three different crystal thicknesses.

Model	Crystal size (mm <sup>3</sup> )	Resolution	RMS	FoV (cm <sup>2</sup> )	S/N-Ratio
		$\langle \text{FWHM} \rangle_{x,y}$ (mm)	$r_{rec} - r_{true}$ (mm)		
Lerche	50×50×10	1.20(15)	0.84(19)	16.4	14(3)
	50×50×20	1.24(10)	0.69(8)	18.9	9(2)
	50×50×30 <sup>(*)</sup>	1.32(20)	0.86(13)	21.6	6(2)
Li	50×50×10	1.24(10)	0.86(23)	18.9	12(5)
	50×50×20	1.46(12)	0.67(4)	21.6	7(3)
	50×50×30 <sup>(*)</sup>	1.43(12)	0.88(16)	21.6	4(2)

(\*) Different cut on  $\chi^2$  (see text).

the 8×8 SiPM matrix of pixels at each event. We have investigated different options for the nodes-structure of the intermediate NN layers and, in general, a single layer of 64 neurons seems to be the best approach in terms of linearity performance and accuracy. Depending on the crystal thickness, typically between  $1.5 \times 10^6$  and  $3 \times 10^6$  events are collected at each position of the 35×35 characterization grid (see Sec. 2). Half of the measured events are used for training the network and the other half are used for the iterative convergence test. With such statistics, and the aforementioned NN structure, approximately 6 minutes are required for each training cycle using a core-i7 processor from Intel. The last layer of the NN consists of just one output neuron ( $x$  or  $y$ ), which represents the corresponding coordinate for the scan position of the 35×35 independent measurements used to train the network (see Sec.2). Before performing the training of the NN the input data-base is pre-filtered by removing events whose charge distribution has a maximum, which is located at least at a distance beyond  $\delta_{df} = 30$  mm from the maximum of the accumulated charge distribution. This allows one to make a more efficient use of the training resources and CPU time by excluding, a priori, a small fraction of stray events or random coincidences (typically 5-10%). We use a total number of 150 epochs to train the NN in order to keep the overall calculation time within reasonable limits. Although generally the network has not fully converged after such a small number of cycles, the margin for further improvement with additional cycles seems rather negligible. Corrections to account for pixel-gain fluctuations seem to play a minor role in NN-based methods, thus we found

no difference between implementing or neglecting such experimental effects. This indicates that the NN seems capable to account itself for gain-inhomogeneities quite reliably along the learning process.

#### *LaCl<sub>3</sub>(Ce) 50×50×10 mm<sup>3</sup>*

Fig. 21 shows the two reference illustrative examples for the NN-approach applied to the 10 mm thick LaCl<sub>3</sub>(Ce) crystal. The improvement in FoV becomes very apparent, when compared to the examples shown in Sec. 3.1, and comparable to the one obtained in the previous section using analytical fit methods.

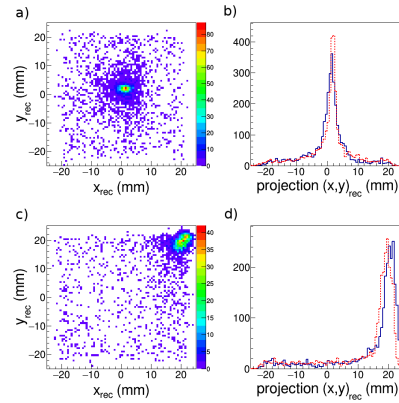


Figure 21: Examples of reconstructed positions with the NN-algorithm for the center of the crystal (a-b) and for a diagonal position shifted 21 mm in  $x$  and  $y$  (c-d) for the 10 mm thick crystal.

The NN approach is particularly sensitive to the details

of the active layers in the neural network. For some of the NN-structures studied the linearity and resolution results were good along some particular direction in the crystal, but unacceptably poor for other directions or regions in the crystal. Therefore it becomes necessary to test the performance of the chosen network layer along the full crystal surface. For this reason the linearity curves for both the central  $x$ - and  $y$ -axis, and for the diagonal scanning line are displayed below in Fig. 22 for the final NN-structure chosen of 64 active neurons in the intermediate layer. The algorithm behaves linear in the range of 46.5 mm both along the central  $x$ - and  $y$ -axis, as well as along the  $x$ - and  $y$ -projections of the crystal diagonal. This leads to an squared FoV of  $\sim 21.6 \text{ cm}^2$ . Within such FoV, the linearity slope is practically 100% along any axis or diagonal. Sudden deviations of the linearity, such as the one occurring at the projected  $x = 10 \text{ mm}$  for the diagonal data-set, lead to localized maximum discrepancies of  $\sim 2 \text{ mm}$ . Most of the remaining discrepancies, both for the diagonal and for the central  $x$ - and  $y$ -axis (Fig. 22), are within about  $\pm 1 \text{ mm}$ , being the average RMS value of  $0.85(5) \text{ mm}$ . The spatial

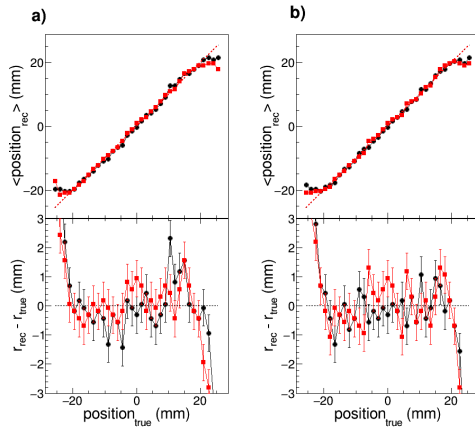


Figure 22: Linearity along the crystal diagonal (a) and horizontal-vertical cross (b) for the 10 mm thick crystal.

resolution is displayed in Fig. 23 for the central-cross of scanned positions along the  $x$ - and  $y$ -axis. On average we find a resolution of  $3.35(11) \text{ mm}$  FWHM for the 10 mm thick crystal. Finally, the NN-algorithm yields an average S/N ratio of  $12.0(2)$ .

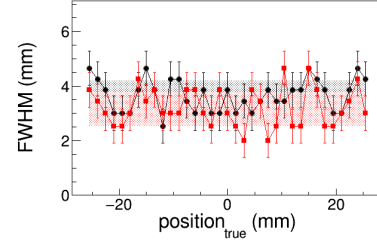


Figure 23: Spatial resolution (FWHM) obtained for the 10 mm crystal along the central  $x$  (black) and  $y$  axis (red). Shadow-bands indicate average values.

### $\text{LaCl}_3(\text{Ce}) 50 \times 50 \times 20 \text{ mm}^3$

Using NNs the quality of the reconstructed 2D-distributions is quite similar to that obtained for the 10 mm thick crystal. This is demonstrated in Fig. 24, which shows the same two scan positions of Fig. 21, as measured and reconstructed now for the 20 mm thick crystal. The linearity curves for the 20 mm thick crys-

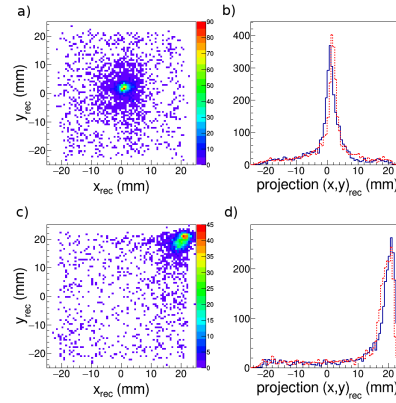


Figure 24: Examples of two position-distributions for the center of the crystal (a-b) and for a diagonal position shifted 21 mm in  $x$  and  $y$  (c-d) for the 20 mm thick crystal.

tal are displayed in Fig. 25 together with the discrepancies related to the ideal-detector performance. The linear range is ascribed to the central  $31 \times 31$  scanned positions, thus yielding also a FoV of  $21.6 \text{ cm}^2$ . The average RMS-deviation found is of  $0.83(6) \text{ mm}$ .

The spatial resolution (see Fig. 26) and the S/N ratio become comparable or slightly better than for the 10 mm

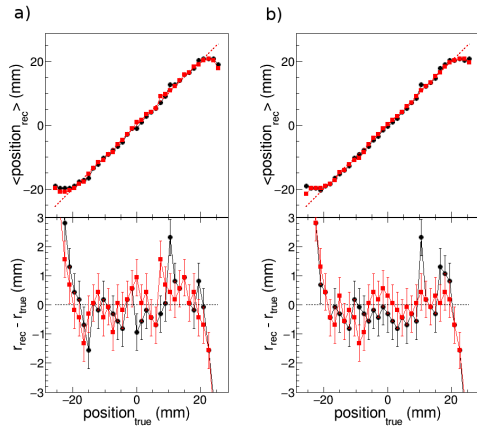


Figure 25: Linearity for the NN-algorithm along the crystal diagonal (a) and the horizontal-vertical cross (b) in the 20 mm thick crystal.

thick crystal, with average values of 3.01(11) mm FWHM and 12.3(4), respectively.

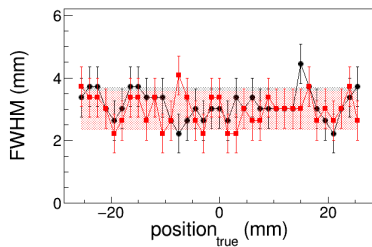


Figure 26: Spatial resolution (FWHM) obtained for the 20 mm crystal along the central  $x$  (black) and  $y$  axis (red) for the 20 mm thick crystal. Shadow-bands indicate average values.

### $LaCl_3(Ce)$ $50 \times 50 \times 30$ mm<sup>3</sup>

The mild differences between the 10 mm and 20 mm thick crystals become now significantly more apparent for the 30 mm thick crystal. The two reference (central and peripheral) 2D-distributions are shown in Fig. 27. The most apparent impact of the crystal thickness is the enhanced border distortion, which can be observed in the linearity curves displayed in Fig. 28. In this case the FoV has to be limited to the central  $28 \times 28$  scanned positions (17.6 cm<sup>2</sup>). Average deviations with respect to the true positions show an average RMS-value of 1.1 mm.

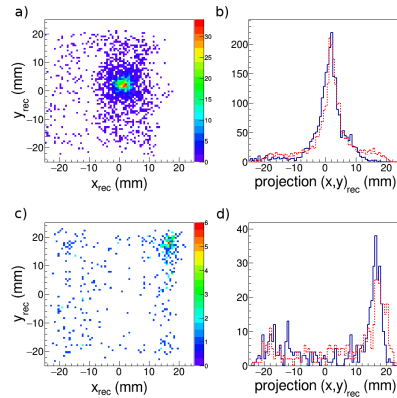


Figure 27: Examples of two position-distributions obtained using the NN-algorithm with the 30 mm thick crystal for the center of the crystal (a) and for the peripheral scan position (b).

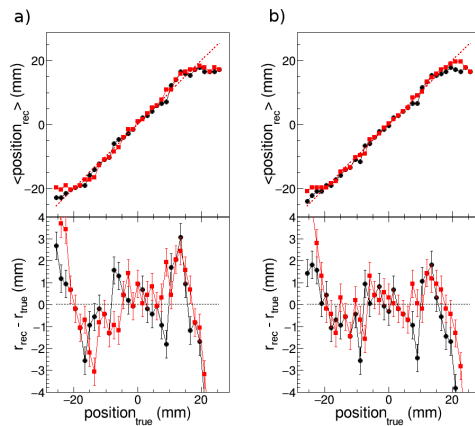


Figure 28: Linearity for the NN-algorithm along the crystal diagonal (a) and central-axes (b) for the 30 mm thick crystal.

In the range of the FoV, the average spatial resolution becomes 3.36(15) mm FWHM (see Fig. 29) and the S/N ratio worsens significantly with an average value of 7.0(4).

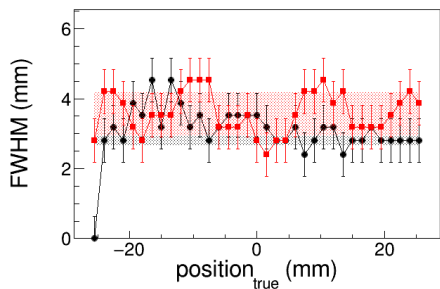


Figure 29: Spatial resolution (FWHM) obtained for the 30 mm crystal along the central  $x$  (black) and  $y$  axis (red). Shadow-bands indicate average values.

#### Summary of performances obtained with NN-based algorithms

The main performance parameters for the NN-based algorithms are summarized below in Table 2. Using NNs the quality of the spatial reconstruction is rather similar for crystal thicknesses of 10 mm and 20 mm, with average position resolutions of  $\sim 3$  mm FWHM over the  $21 \text{ cm}^2$  FoV. On the other hand, the 30 mm thick crystal shows a comparable performance in terms of resolution ( $\sim 3.4$  mm FWHM) but the FoV is reduced to 81% of the field attainable with the thinner crystals. In terms of processing speed, the NN-algorithm performance is quite high (5200(400) Events/s), about 76% of the Anger-algorithm processing rate  $r_{Anger}$  (see Sec. 3.1). Other aspects about the performance found for the NN-algorithm will be discussed below in Sec.5 in the context of a comparison with the analytical methods.

#### 4. Depth of Interaction (DoI)

Initially we started to research a self-consistent approach, where all three space coordinates  $x, y$  and  $z$  were included in the position-reconstruction analysis, both for the analytical-fit and for the NN-based algorithms of Sec. 3.2 and Sec. 3.3, respectively. However, we have found similar or better performances in both cases, when

decoupling the position reconstruction in the transversal  $(x, y)$ -plane from the DOI analysis. To some extent, this may be related to the nature of the problem because a much higher-sensitivity and precision is expected for the  $x, y$ -coordinates than for  $z$ . In the former case variations on the first momentum of the distributions are very well estimated by the position of its maximum over the full detector surface. In the second case, however, only small changes in the second momentum are perceivable in the measured distribution, at least with the used instrumentation and SiPM pixelation.

Thus, in order to determine the DoI for the  $\gamma$ -ray hit we use a rather phenomenological approach based on the inverse dependency of the  $z$ -coordinate (measured from the entrance surface) with the second momentum of the scintillation distribution. Neglecting perturbations induced by reflection effects we assume an inverse-linear relationship between DOI and the cross-section of the distribution  $A_w$  at a given height  $h_w$ . This assumption is naturally expected from the parameterizations reported e.g. in Refs.[8, 24]. We choose  $h_w$  the half-maximum value for each particular event. Smaller  $h_w$  values are significantly affected by background light and spurious fluctuations. A higher choice for  $h_w$  becomes less sensitive to the DOI because then the measured distribution width starts to be dominated by the size of the pixel (6 mm). In order to avoid artifacts in the reconstructed DOI arising from the 6 mm wide sampling resolution before computing  $A_w$  for each measured event we perform a linear interpolation onto a 1 mm grid. Because DOI is more relevant for thick crystals, we focus here on the  $\text{LaCl}_3(\text{Ce})$  with size of  $50 \times 50 \times 30 \text{ mm}^3$ . Our linear assumption for the DOI calibration is well justified, as demonstrated in Fig. 30, where the measured values for  $A_w$  at half maximum (already calibrated) are compared against MC calculated DOIs. Ideal simulated DOI values are shown by the black distribution in Fig. 30. The data used in this comparison corresponds to the central scan position  $x = 0$  mm and  $y = 0$  mm, where border effects can be safely neglected. The prominent peak in the experimental distribution arises from  $\gamma$ -ray hits near the optical window (large DOIs), where most of the charge above  $h_w$  is concentrated in just one single pixel of the Si-PM. This leads to a slight overestimation of events with large DOI-values. The latter represents a less than 10% of the total measured events. This artifact could be reduced by lowering the value of  $h_w$ , neverthe-

Table 2: Summary of the performance results obtained with NN-based algorithms for the three different PSDs.

Crystal size (mm <sup>3</sup> )	Resolution < FWHM > <sub>(x,y)</sub> (mm)	RMS $r_{rec} - r_{true}$ (mm)	FoV (cm <sup>2</sup> )	S/N-Ratio
50×50×10	3.35(11)	0.86(7)	21.6	12.0(2)
50×50×20	3.01(11)	0.83(6)	21.6	12.3(4)
50×50×30	3.4(11)	0.94(16)	17.6	7.0(4)

less at the cost of higher incertitude on the estimated DOI.

In order to estimate an uncertainty for the experimentally determined DoI, we compare its distribution with respect to the values obtained from a broadened MC-simulation. The result shown below in Fig. 30 corresponds to a broadening Gaussian function with a width of 10 mm FWHM. Thus, a  $\pm 4$  mm represents a reasonable estimate for the RMS uncertainty on the DOI.

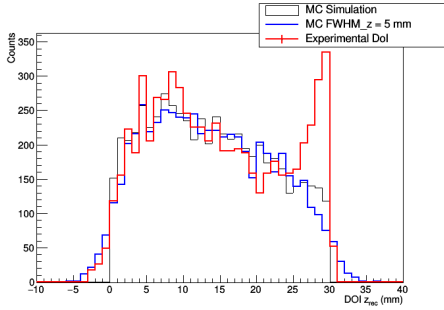


Figure 30: DOI-calibrated area ( $A_w$ ) at half maximum calibrated (red distribution). MC simulation of DOI values without broadening (black histogram) and with 10 mm FWHM broadening (blue histogram).

For peripheral  $\gamma$ -ray hits in the crystal the width and the shape of the scintillation-light distribution depends not only on the DoI, but also on reflection effects. Thus, we use the 35×35 scanned positions (see Sec. 2) in order to determine, at each of them, i.e. on a grid of 1.5 mm×1.5 mm the  $A_w$  values for the broadest and narrowest light distributions at half maximum, which are assigned to DoI = 0 mm and DoI = 30 mm, respectively. A linear regression is calculated for each scan position in order to interpolate any intermediate value for the DoI. DoI reconstruction examples for scan positions at the center and at the corner of the 30 mm thick crystal are shown

below in Fig. 31.

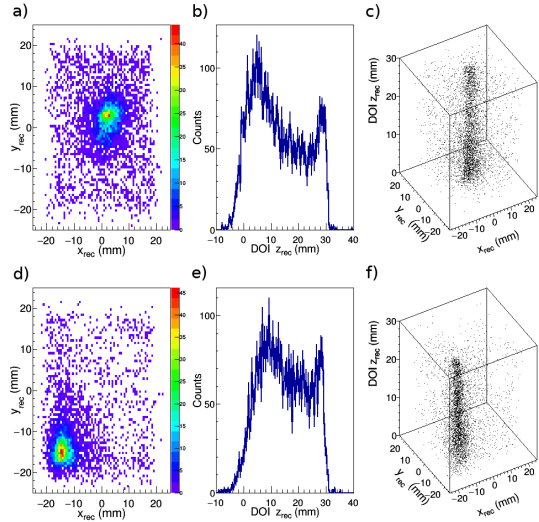


Figure 31: Examples of reconstructed DOI coordinates for the central scan position (a-c) and for a peripheral scan position (d-f). In each case the 2D  $(x, y)$  positions as reconstructed using a NN-algorithm are shown (a,d) and the corresponding calibrated DOI distributions are shown in panels (b,e). The distribution of 3D-coordinates is shown in (c,f).

The list of 35×35 linear-regression coefficients are then stored in a single file for each crystal thickness. For an arbitrary measurement, the corresponding DOI-calibration coefficients and invoked after the  $(x, y)$  coordinates have been determined either using the analytical or the NN-approach. In summary, one can conclude that this is a rather simple, yet reliable approach for determining the DOI at each  $(x, y)$ -point of the crystal, with an uncertainty of  $\pm 4$  mm RMS. Similar results are obtained for the 10 mm and 20 mm thick crystals.

## 5. Summary and outlook

The main performance features found for the different position-reconstruction algorithms have been summarized in Table 1 and Table 2. The main features are displayed graphically in Fig. 32. An interesting result which derives from this study is that, for all methods studied, the crystal thickness has a small impact in the position accuracy, whereas its effect is more sizeable in terms of linearity, FoV and S/N-ratio. With respect to the position reconstruction accuracy the analytical-fit methods show a superior performance (on average three times better than NN-algorithms), however at the cost of reconstruction efficiency (and CPU-resources). On the other hand, the NN-algorithm shows a remarkable performance in terms of linearity, FoV and reconstruction speed, but it seems to be more limited in terms of the attainable spatial resolution. Compared to analytical methods, NN-algorithms seem also quite promising for position reconstruction in thick (20-30 mm) crystals, as it can be inferred from the S/N-ratios displayed in Fig. 32.

With respect to the applicability of these results in the field of neutron capture measurements, and in particular in the framework of the HYMNS project, the loss of reconstruction efficiency by the analytic-fit methods seems to be a major drawback. Indeed, a  $\sim 50\%$  and  $\sim 20\%$  of efficiency for the scatter- and absorber-detectors of i-TED would imply an overall reduction by nearly a factor of 10 in terms of counting statistics, which would be rather prohibitive in this kind of experiments. This limitation can be fully avoided if a NN-algorithm is employed for the position reconstruction. As it has been demonstrated, NN algorithms show a similar FoV and, on average, better S/N ratios than analytic methods. At this moment, the  $\sim 3$  mm FWHM spatial resolution attainable with NN-algorithms does not seem a limiting factor in terms of the Compton background rejection algorithms, given that the related uncertainty is still dominated by the energy resolution of  $\text{LaCl}_3(\text{Ce})$  crystals.

### Acknowledgment

This work has received funding from the European Research Council (ERC) under the European Union's Horizon 2020 research and innovation programme (ERC Consolidator Grant project HYMNS, with grant agreement

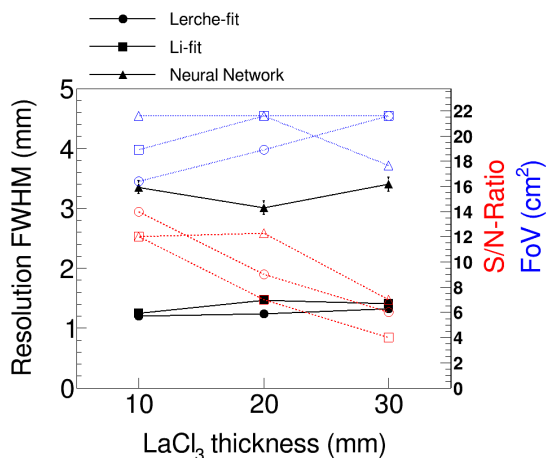


Figure 32: Solid symbols represent the spatial resolution attained with the different position reconstruction techniques (see legend). Empty symbols represent the average S/N-Ratio and FoV (see label) obtained in each case.

nr. 681740). The authors acknowledge the Spanish Ministerio de Ciencia e Innovación under grants FPA2014-52823-C2-1-P, FPA2017-83946-C2-1-P and the program Severo Ochoa (SEV-2014-0398) for support. CDP acknowledges CSIC funds from PIE-201750I026. We would like to thank PETSys Electronics S.A. for technical support and helpful collaboration with the I3M-Institute at the Polytechnical University of Valencia.

### References

- [1] High-sensitivity Measurements of key stellar Nucleo-Synthesis reactions (HYMNS), ERC-Consolidator Grant Agreement No. 681740.
- [2] C. Domingo-Pardo. i-TED: A novel concept for high-sensitivity (n, $\gamma$ ) cross-section measurements. *Nuclear Instruments and Methods in Physics Research A*, 825:78–86, July 2016.
- [3] D.L. Pérez Magán, L. Caballero-Ontanaya, C. Domingo-Pardo, J. Agramunt-Ros, F. Albiol, A. Casanovas, A. González, C. Guerrero, J. Leredegui-Marco, A. Tarifeño-Saldivia, and the n\_TOF Collaboration. First tests of the applicability of  $\gamma$ -ray imaging for background discrimination in

- time-of-flight neutron capture measurements. *ArXiv e-prints*, October 2015.
- [4] C. Guerrero, A. Tsinganis, E. Berthoumieux, M. Barbagallo, F. Belloni, F. Gunsing, C. Weiß, E. Chiaveri, M. Calviani, V. Vlachoudis, S. Altstadt, S. Andriamonje, J. Andrzejewski, L. Audouin, V. Bécares, F. Bečvář, J. Billowes, V. Boccone, D. Bosnar, M. Brugger, F. Calviño, D. Cano-Ott, C. Carrapiço, F. Cerutti, M. Chin, N. Colonna, G. Cortés, M. A. Cortés-Giraldo, M. Diakaki, C. Domingo-Pardo, I. Duran, R. Dressler, N. Dzyziuk, C. Eleftheriadis, A. Ferrari, K. Fraval, S. Ganesan, A. R. García, G. Giubrone, K. Göbel, M. B. Gómez-Hornillos, I. F. Gonçalves, E. González-Romero, E. Griesmayer, P. Gurusamy, A. Hernández-Prieto, P. Gurusamy, D. G. Jenkins, E. Jericha, Y. Kadi, F. Käppeler, D. Karadimos, N. Kivel, P. Koehler, M. Kokkoris, M. Krtička, J. Kroll, C. Lampoudis, C. Langer, E. Leal-Cidoncha, C. Lederer, H. Leeb, L. S. Leong, R. Losito, A. Manousos, J. Marganec, T. Martínez, C. Massimi, P. F. Mastinu, M. Mastromarco, M. Meaze, E. Mendoza, A. Mengoni, P. M. Milazzo, F. Mingrone, M. Mirea, W. Mondalaers, T. Papaevangelou, C. Paradela, A. Pavlik, J. Perkowski, A. Plompen, J. Praena, J. M. Quesada, T. Rauscher, R. Reifarh, A. Riego, F. Roman, C. Rubbia, M. Sabate-Gilarte, R. Sarmiento, A. Saxena, P. Schillebeeckx, S. Schmidt, D. Schumann, P. Steinegger, G. Tagliente, J. L. Tain, D. Tarrío, L. Tassan-Got, S. Valenta, G. Vannini, V. Variale, P. Vaz, A. Ventura, R. Versaci, M. J. Vermeulen, R. Vlastou, A. Wallner, T. Ware, M. Weigand, T. Wright, and P. Žugec. Performance of the neutron time-of-flight facility n\_TOF at CERN. *European Physical Journal A*, 49:27, February 2013.
- [5] P. Olleros, L. Caballero, C. Domingo-Pardo, V. Babiano, I. Ladarescu, D. Calvo, P. Gramage, E. Nacher, J. L. Tain, and A. Tolosa. On the performance of large monolithic LaCl<sub>3</sub>(Ce) crystals coupled to pixelated silicon photosensors. *ArXiv e-prints*, January 2018.
- [6] H. O. Anger. Scintillation Camera. *Review of Scientific Instruments*, 29:27–33, January 1958.
- [7] H. O. Anger. Sensitivity, Resolution, and Linearity of the Scintillation Camera. *IEEE Transactions on Nuclear Science*, 13:380–392, December 1966.
- [8] C. W. Lerche, J. M. Benlloch, F. Sánchez, N. Pavón, N. Giménez, M. Fernández, M. Giménez, A. Sebastián, J. Martínez, and F. J. Mora. Depth of interaction detection with enhanced position-sensitive proportional resistor network. *Nuclear Instruments and Methods in Physics Research A*, 537:326–330, January 2005.
- [9] P. Vaska, M. J. Petrillo, and G. Muehllehner. Virtual PMTs: improving centroid positioning performance near the edges of a gamma camera detector. *IEEE Transactions on Nuclear Science*, 48:645–649, June 2001.
- [10] R. Pani, F. Vittorini, M. N. Cinti, P. Bennati, R. Pellegrini, S. Ridolfi, R. Scafè, S. Lo Meo, M. Mattioli, F. L. Navarra, G. Moschini, A. Fabbri, E. D’Abramo, V. Orsolini Cencelli, and D. Sacco. Revisited position arithmetics for LaBr<sub>3</sub>:Ce continuous crystals. *Nuclear Physics B Proceedings Supplements*, 197:383–386, December 2009.
- [11] E. V. D. van Loef, P. Dorenbos, C. W. E. van Eijk, K. W. Krämer, and H. U. Güdel. Scintillation properties of LaBr<sub>3</sub>:Ce<sup>3+</sup> crystals: fast, efficient and high-energy-resolution scintillators. *Nuclear Instruments and Methods in Physics Research A*, 486:254–258, June 2002.
- [12] K. S. Shah, J. Glodo, M. Klugerman, W. W. Moses, S. E. Derenzo, and M. J. Weber. Labr/sub 3/:ce scintillators for gamma-ray spectroscopy. *IEEE Transactions on Nuclear Science*, 50(6):2410–2413, Dec 2003.
- [13] K. S. Shah, J. Glodo, W. Higgins, E. V. D. van Loef, W. W. Moses, S. E. Derenzo, and M. J. Weber. Cebr/sub 3/ scintillators for gamma-ray spectroscopy. *IEEE Transactions on Nuclear Science*, 52(6):3157–3159, Dec 2005.

- [14] W. W. Moses and K. S. Shah. Potential for RbGd<sub>2</sub>Br<sub>7</sub>:Ce, LaBr<sub>3</sub>:Ce, LaBr<sub>3</sub>:Ce, and LuI<sub>3</sub>:Ce in nuclear medical imaging. *Nuclear Instruments and Methods in Physics Research A*, 537:317–320, January 2005.
- [15] J. J. Vaquero, J. J. Snchez, E. Lage, J. M. Udas, P. Guerra, and M. Desco. Design of doi pet detector modules using phoswich and sipms: First results. In *2011 IEEE Nuclear Science Symposium Conference Record*, pages 3311–3313, Oct 2011.
- [16] M. Grodzicka-Kobylka, T. Szczesniak, M. MoszyÅski, L. Swiderski, and M. SzawÅowski. Silicon photomultipliers in scintillation detectors used for gamma ray energies up to 6.1 mev. *Nuclear Instruments and Methods in Physics Research Section A: Accelerators, Spectrometers, Detectors and Associated Equipment*, 874:137 – 148, 2017.
- [17] A.N. Saxena. Monolithic concept and inventions of integrated circuits by kilby and noyce. In *NSTI-Nanotech*, volume 3, pages 460–469, 2007. Nano Science and Technology Institute Annual Conference.
- [18] S. Blin, P. Barrillon, and C. de La Taille. Maroc, a generic photomultiplier readout chip. In *IEEE Nuclear Science Symposium Medical Imaging Conference*, pages 1690–1693, Oct 2010.
- [19] I. Sacco, P. Fischer, and M. Ritzert. PETA4: a multi-channel TDC/ADC ASIC for SiPM readout. *Journal of Instrumentation*, 8:C12013, December 2013.
- [20] Agostino Di Francesco, Ricardo Bugalho, Luis Oliveira, Angelo Rivetti, Manuel Rolo, Jose C. Silva, and Joao Varela. TOFPET 2: A high-performance circuit for PET time-of-flight. *Nuclear Instruments and Methods in Physics Research A*, 824:194–195, July 2016.
- [21] A. J. Bird, Z. He, and D. Ramsden. Multi-channel readout of crossed-wire anode photomultipliers. *Nuclear Instruments and Methods in Physics Research A*, 348:668–672, September 1994.
- [22] A. Truman, A. J. Bird, D. Ramsden, and Z. He. Pixellated CsI(Tl) arrays with position-sensitive PMT readout. *Nuclear Instruments and Methods in Physics Research A*, 353:375–378, December 1994.
- [23] T. Ling, T. H. Burnett, T. K. Lewellen, and R. S. Miyaoka. Parametric positioning of a continuous crystal pet detector with depth of interaction decoding. *Physics in Medicine & Biology*, 53(7):1843, 2008.
- [24] Z. Li, M. Wedrowski, P. Bruyndonckx, and G. Vandersteen. Nonlinear least-squares modeling of 3D interaction position in a monolithic scintillator block. *Physics in Medicine and Biology*, 55:6515–6532, November 2010.
- [25] C. Domingo-Pardo, N. Goel, T. Engert, J. Gerl, M. Isaka, I. Kojouharov, and H. Schaffner. A position sensitive gamma-ray scintillator detector with enhanced spatial resolution, linearity, and field of view. *IEEE Transactions on Medical Imaging*, 28(12):2007–2014, December 2009.
- [26] J. Cabello, P. Barrillon, J. Barrio, M. G. Bisogni, A. Del Guerra, C. Lacasta, M. Rafecas, H. Saikouk, C. Solaz, P. Solevi, C. de La Taille, and G. Llosá. High resolution detectors based on continuous crystals and SiPMs for small animal PET. *Nuclear Instruments and Methods in Physics Research A*, 718:148–150, August 2013.
- [27] M. C. Maas, D. J. van der Laan, D. R. Schaart, J. Huizenga, J. C. Brouwer, P. Bruyndonckx, S. Leonard, C. Lemaitre, and C. W. E. van Eijk. Experimental Characterization of Monolithic-Crystal Small Animal PET Detectors Read Out by APD Arrays. *IEEE Transactions on Nuclear Science*, 53:1071–1077, June 2006.
- [28] H. T. van Dam, S. Seifert, R. Vinke, P. Dendooven, H. Lohner, F. J. Beekman, and D. R. Schaart. Improved nearest neighbor methods for gamma photon interaction position determination in monolithic scintillator pet detectors. *IEEE Transactions on Nuclear Science*, 58(5):2139–2147, Oct 2011.
- [29] S. Aldawood, P. G. Thirolf, A. Miani, M. Böhmer, G. Dedes, R. Gernhäuser, C. Lang, S. Liprandi, L. Maier, T. Marinšek, M. Mayerhofer, D. R.

- Schaart, I. V. Lozano, and K. Parodi. Development of a Compton camera for prompt-gamma medical imaging. *Radiation Physics and Chemistry*, 140:190–197, November 2017.
- [30] S. Liprandi, M. Mayerhofer, S. Aldawood, T. Binder, G. Dedes, A. Miani, D. Schaart, I. Valencia Lozano, K. Parodi, and P. Thirolf. Sub-3mm spatial resolution from a large monolithic LaBr<sub>3</sub> (Ce) scintillator. *Current Directions in Biomedical Engineering*, 3:655–659, February 2017.
- [31] F. Mateo, R. J. Aliaga, N. Ferrando, J. D. Martínez, V. Herrero, C. W. Lerche, R. J. Colom, J. M. Monzó, A. Sebastiá, and R. Gadea. High-precision position estimation in PET using artificial neural networks. *Nuclear Instruments and Methods in Physics Research A*, 604:366–369, June 2009.
- [32] P. Bruyndonckx, C. Lemaître, D. Schaart, M. Maas, D. J. van der Laan, M. Krieguer, O. Devroede, and S. Tavernier. Investigation of an in situ position calibration method for continuous crystal-based PET detectors. *Nuclear Instruments and Methods in Physics Research A*, 571:304–307, February 2007.
- [33] A. Gostojić, V. Tatischeff, J. Kiener, C. Hamadache, J. Peyré, N. Karkour, D. Linget, L. Gibelin, X. Lafay, X. Grave, N. Dosme, E. Legay, S. Blin, and P. Barrillon. Characterization of LaBr<sub>3</sub>:Ce and CeBr<sub>3</sub> calorimeter modules for 3D imaging in gamma-ray astronomy. *Nuclear Instruments and Methods in Physics Research A*, 832:24–42, October 2016.
- [34] P. Conde, A. Iborra, A. J. Gonzalez, L. Hernandez, P. Bellido, L. Moliner, J. P. Rigla, M. J. Rodriguez-Ivarez, F. Sanchez, M. Seimetz, A. Soriano, L. F. Vidal, and J. M. Benlloch. Determination of the interaction position of gamma photons in monolithic scintillators using neural network fitting. *IEEE Transactions on Nuclear Science*, 63(1):30–36, Feb 2016.
- [35] A. Ulyanov, O. Morris, O. J. Roberts, I. Tobin, L. Hanlon, S. McBreen, D. Murphy, N. Nelms, and B. Shortt. Localisation of gamma-ray interaction points in thick monolithic CeBr<sub>3</sub> and LaBr<sub>3</sub>:Ce scintillators. *Nuclear Instruments and Methods in Physics Research A*, 844:81–89, February 2017.
- [36] <http://sensl.com/documentation>.
- [37] A. Di Francesco, R. Bugalho, L. Oliveira, A. Rivetti, M. Rolo, J. C. Silva, and J. Varela. TOFPET 2: A high-performance circuit for PET time-of-flight. *Nuclear Instruments and Methods in Physics Research A*, 824:194–195, July 2016.
- [38] <http://www.arrickrobotics.com/>.
- [39] S. Agostinelli, J. Allison, K. Amako, J. Apostolakis, H. Araujo, P. Arce, M. Asai, D. Axen, S. Banerjee, G. Barrand, F. Behner, L. Bellagamba, J. Boudreau, L. Broglia, A. Brunengo, H. Burkhardt, S. Chauvie, J. Chuma, R. Chytracsek, G. Cooperman, G. Cosmo, P. Degtyarenko, A. Dell’Acqua, G. Depaola, D. Dietrich, R. Enami, A. Feliciello, C. Ferguson, H. Fesefeldt, G. Folger, F. Foppiano, A. Forti, S. Garelli, S. Giani, R. Giannitrapani, D. Gibin, J. J. Gómez Cadenas, I. González, G. Gracia Abril, G. Greeniaus, W. Greiner, V. Grichine, A. Grossheim, S. Guatelli, P. Gumplinger, R. Hamatsu, K. Hashimoto, H. Hasui, A. Heikkinen, A. Howard, V. Ivanchenko, A. Johnson, F. W. Jones, J. Kallenbach, N. Kanaya, M. Kawabata, Y. Kawabata, M. Kawaguti, S. Kelner, P. Kent, A. Kimura, T. Kodama, R. Kokoulin, M. Kossov, H. Kurashige, E. Lamanna, T. Lampén, V. Lara, V. Lefebure, F. Lei, M. Liendl, W. Lockman, F. Longo, S. Magni, M. Maire, E. Medernach, K. Minamimoto, P. Mora de Freitas, Y. Morita, K. Murakami, M. Nagamatu, R. Nartallo, P. Nieminen, T. Nishimura, K. Ohtsubo, M. Okamura, S. O’Neale, Y. Oohata, K. Paech, J. Perl, A. Pfeiffer, M. G. Pia, F. Ranjard, A. Rybin, S. Sadilov, E. Di Salvo, G. Santin, T. Sasaki, N. Savvas, Y. Sawada, S. Scherer, S. Sei, V. Sirotenko, D. Smith, N. Starkov, H. Stoecker, J. Sulkimo, M. Takahata, S. Tanaka, E. Tcherniaev, E. Safai Tehrani, M. Tropeano, P. Truscott, H. Uno, L. Urban, P. Urban, M. Verderi, A. Walkden, W. Wander, H. Weber, J. P. Wellisch, T. Wenaus, D. C. Williams, D. Wright, T. Yamada, H. Yoshida, D. Zschesche, and G. EANT4 Collaboration. GEANT4 a simulation toolkit. *Nuclear Instruments and Methods in Physics Research A*, 506:250–303, 2003.

- [40] R. Brun and F. Rademakers. ROOT—An object oriented data analysis framework. *Nuclear Instruments and Methods in Physics Research A*, 389:81–86, February 1997.